Organic photodetector with built-in amplification for the detection of visible light with low optical power.

*Xiaojia Jia, Canek Fuentes-Hernandez, Wen-Fang Chou, Bernard Kippelen**

Center for Organic Photonics and Electronics (COPE), School of Electrical and Computer Engineering, Georgia Institute of Technology, Atlanta, Georgia 30332, USA.

*Corresponding author. E-mail: kippelen@ece.gatech.edu

This document is a copy of the manuscript accepted for publication in the journal *Organic Electronics.* Doi: 10.1016/j.orgel.2021.106064

Organic photodetector with built-in amplification for the detection of visible light with low optical power.

*Xiaojia Jia, Canek Fuentes-Hernandez, Wen-Fang Chou, Bernard Kippelen**

Center for Organic Photonics and Electronics (COPE), School of Electrical and Computer Engineering, Georgia Institute of Technology, Atlanta, Georgia 30332, USA. *Corresponding author. E-mail: kippelen@ece.gatech.edu

Abstract:

We report on an organic-based photodetector device that integrates a dual-gate organic thin-film transistor (DG-OTFT) with an organic photodiode (OPD) to produce a device with a high effective responsivity at low optical power and video-rate compatible response. In this device, the OPD operates in photovoltaic mode, instead of the commonly used photoconductive model, to modulate one of the gate voltages of the DG-OTFT. Effective responsivity values of 10 A W^{-1} are measured at optical power values lower than 10 nW at 635 nm. Modeling of the operation of this new photodetector suggests that effective responsivity values up to 10^5 A W^{-1} can be achieved at optical powers of 1 nW using current printing technology and state-of-the-art organic semiconductors.

1. Introduction:

The detection of weak optical signals is of technological importance for a wide range of applications, from consumer electronics, health and radiation monitoring systems, to security, and the internet of things [1-4]. Photodetectors with a high specific detectivity (D^*) are able to detect such signals, but they are generally based on crystalline inorganic semiconductors processed at high temperatures on rigid substrates [5, 6]. This imposes cost tradeoffs that prevent their wide-spread distribution. Low-cost large-area flexible photodetectors that consume low electrical power and with a high D^* will be critical to enable ubiquitous distribution of highly sensitive light sensors in these emerging applications [1, 6-8]. As a reminder, D^* is defined by the ratio: $\sqrt{AB}\,NEP^{-1}$, where A is the photodetector area, B is the measurement bandwidth and NEP is noise equivalent power representing the minimum detectable optical power that produces a signal-to-noise ratio of one.

Organic photodetectors are promising in this context because they can be processed at low temperatures (< 150 °C), are lightweight, and can be made flexible. Recently, organic photodiodes (OPDs) have achieve noise equivalent power values (NEP) as low as a few hundreds of fW in the visible spectral range and specific detectivity (D^*) values ca. 10^{12} Jones at $B = 1.5$ Hz, representing a level of performance that is comparable to that of state-of-the-art low-noise Si photodiodes (SiPDs) [7].

Because the external quantum efficiency (EQE) of photodiodes is typically smaller than 100%, their responsivity ($R = I_{ph}\,\phi_{opt}^{-1}$) values are of 100's of mA W^{-1} in the visible spectral range, yielding very small photogenerated currents in response to weak optical signals [9-12]. For instance, an optical signal with a power of 1 nW will produce a photocurrent ca. 100's pA in a

photodiode. To measure such small photocurrent values, external amplification using an operational amplifier could be used [6]. Although internal amplification through impact ionization has become a preferable approach to achieve detection of weak optical signals using inorganic photodetectors, in OPDs, impact ionization has not been observed and internal amplification mechanisms have been restricted to photoconductive gain due to the presence of traps. Photoconductive gain in OPDs has yield responsivity values up to 10^5 A W^{-1} with a dynamic response that is typically not video-rate compatible, aside from a few exceptions [13]. Organic phototransistors (OPTs) have also shown EQE values larger than 100%, and responsivity values up to 1,000 A W^{-1} [14]. OPTs take advantage of the transistor's gate modulation [15] to amplify the photovoltage that is generated in its channel, or to show photoconductive gain, but also show response times in the 0.1 to 100 s range [16-20].

In this work, a photodetector architecture is proposed that integrates a dual-gate organic thin-film transistor (DG-OTFT) with an OPD. The operational principle of this device is based on the generation of a photovoltage (or open-circuit voltage (V_{OC})) produced by an OPD under illumination that is applied to the bottom gate of a DG-OTFT, thereby modulating the channel current flowing in the transistor. Operated in saturation mode, the DG-OTFT provides a transduction of the OPD's photovoltage to ease the detection of weak optical signals. Consequently, this approach is different to previous demonstrations wherein an OPD is connected to the source electrode of an OTFT [21]. This photodetector geometry also enables video-rate compatible photoresponse times (ca. 15 ms), which are faster than typical values reported in OPTs or OPDs with photoconductive gain. This approach builds on the recent demonstration of OTFTs that exhibit operational and environmental stability comparable to other commercial TFT technologies [22] through the use of an ultra-thin bilayer gate dielectric comprised of an amorphous

fluoropolymer CYTOP layer and a nanolaminate (NL) of metal oxide layer grown by atomic layer deposition (ALD) [22-24] and on the recent demonstration of large-area low-noise OPDs with performance metrics that are comparable to those of silicon for the detection of visible light [25]. To rationalize the experimental results, an analytical model that quantitatively describes the measured data was developed and validated. Using this model, effective responsivity values up to 10^5 A W^{-1} are predicted at optical powers as low as 1 nW.

2. Experimental

2.1 Device fabrication

Devices were fabricated on commercially available ITO-coated glass substrates with a sheet resistance of 9-15 Ω/□ (Colorado Concepts) cut into 1.5" x 2" pieces. The ITO was partially masked with Kapton® tapes and patterned by wet etching with a 3:1 volume ratio of HNO_3: HCl solution for 8 min at a bath temperature of 60 °C. After etching, the patterned slides were rinsed with distilled water and scrubbed with detergent (Alconox Liquinox), and then were solvent cleaned in sequential ultrasonic baths of deionized water, acetone, and 2-propanol at a temperature of 65 °C for at least 30 min for each step.

Poly(dimethylsiloxane) (PDMS) masks were used during the solution process of the DG-OTFT and the OPD, respectively. To fabricate the PDMS masks, a solution of 1:1 weight ratio of base and agent (Gelest OE™ 41) was gently poured onto a flat glass mold without any trapped air bubbles, and then cured at 80 °C for 1 h under atmospheric pressure. After cooling down, the PDMS film was peeled off and cut into the size of 1.5" x 1.3" and 1.5" x 0.7" for covering the OTFT area and the OPD area, respectively.

During the fabrication of the OPD, the OTFT area was covered with the PDMS mask. A 0.4 wt.% polyethylenimine ethoxylated (PEIE, Sigma Aldrich) solution was prepared in 2-

methoxyethanol (Sigma Aldrich) and spun on each of the substrates at 5,000 rpm with 928 rpm s^{-1} acceleration for 60 s through a 0.2 μm polytetrafluoroethylene (PTFE) filter (VWR), followed by thermal annealing on a hot plate at 100 °C for 10 min in air. The PEIE-coated ITO substrates were transferred into a N_2-filled glovebox for the next processes. A solution of 1:1 weight ratio of poly(3-hexylthiophene-2,5-diyl) (P3HT, Rieke Metals) and indene-C_{60} bisadduct (ICBA, Luminescence Technology) was prepared in 1,2-dichlorobenzene (Sigma Aldrich) for a total concentration of 100 mg mL^{-1} and was placed on a hot plate at 70 °C and set to magnetically stir at 500 rpm for 12 h inside a N_2-filled glovebox. P3HT: ICBA was spun on top of the PEIE-coated substrates at 800 rpm with 10,000 rpm s^{-1} acceleration for 30 s through a 0.2 μm PTFE filter. The films were solvent annealed for 5 h and then thermal annealed at 150 °C for 10 min in a N_2-filled glovebox. In a high-vacuum thermal evaporation system (Kurt J. Lesker SPECTROS), 10 nm-thick MoO_3 and 150 nm-thick Ag were deposited on the P3HT: ICBA layer in sequence through a shadow mask, at a base pressure of $< 5 \times 10^{-7}$ Torr at room temperature, to form the top electrodes of the OPDs. The top electrodes were extended with aluminum conductive tapes (3M™ 1170 tape), and the PDMS mask was removed from the OTFT area. After a 50 nm-thick Al_2O_3 layer was deposited on the substrate as a bottom gate dielectric layer of the DG-OTFT in a Savannah 100 ALD system (Cambridge Nanotech) at 110 °C, the OPD area was covered with Kapton® tape. Then, 50 nm-thick Ag was deposited through a shadow mask to form the source and drain electrodes in a Kurt J. Lesker SPECTROS thermal evaporator at a deposition rate of 1 Å s^{-1} under 5×10^{-7} Torr at room temperature. Then, the OPD area was covered by the PDMS mask before spin coating the OTFT semiconductor layer. To form a self-assembled monolayer (SAM) of pentafluorobenzenthiol (PFBT) on Ag electrodes, a 100 mM PFBT solution was prepared by dissolving in 1,2,3,4-tetrahydronaphthalene anhydrous (tetralin, Sigma Aldrich). A 1:1 weight

ratio of poly[bis(4-phenyl)(2,4,6-trimethylphenyl)amine] (PTAA, Sigma Aldrich) and 6,13-bis(triisopropylsilylethynyl)pentacene (TIPS-pentacene, Sigma Aldrich) blend was dissolved in tetralin for a concentration of 30 mg mL^{-1}. 10 mM PFBT-mixed TIPS/PTAA solution was then prepared by mixing 100 mM PFBT solution in TIPS/PTAA solution in a volume ratio of 1: 9. A 70 nm-thick active semiconducting layer was deposited by spin-coating PFBT-mixed TIPS/PTAA solution (filtered with a 0.2 μm PTFE filter) at 500 rpm for 10 s with 500 rpm s^{-1} acceleration and 2,000 rpm for 20 s with 1,000 rpm s^{-1} acceleration, followed by annealing at 100 ºC on a hot plate for 15 min in a N_2-filled glove box. The as-purchased 9 wt.% CYTOP (ASAHI GLASS, CTL-890M) was diluted with the solvent (ASAHI GLASS, CT-SOLV180) in a 1:3.5 volume ratio to have a 2 wt.% CYTOP solution, which was spun coat on top of the semiconductor layer at 3,000 rpm for 60 s with 10,000 rpm s^{-1} acceleration, followed by annealing at 100 ºC for 10 min on a hot plate in a N_2-filled glove box. The final thickness of CYTOP film was 35 nm. After removing the PDMS mask from the OPD area, a 33 nm-thick Al_2O_3-HfO_2 NL was deposited in the ALD system by alternating 5 cycles of Al_2O_3 and 5 cycles of HfO_2 for 30 times at 110 ºC. Finally, the top-gate electrodes (100 nm-thick Ag) were deposited through a shadow mask, using a Kurt J. Lesker SPECTROS thermal evaporator at a deposition rate of 1 Å s^{-1} at a base pressure of $< 5 \times 10^{-7}$ Torr at room temperature.

2.2 Device characterization

The capacitance density of the top and bottom gate dielectric layers of DG-OTFT was measured by an Agilent 4284A LCR meter in capacitors with Ag electrodes. The value of capacitance density was extracted from measurements of nine capacitors with different area. The capacitance density values are 37.2 nF cm^{-2} and 150.6 nF cm^{-2} for the top gate dielectric layer (CYTOP/NL) and the bottom gate dielectric layer (Al_2O_3), respectively. The measurement setup for the electrical and

optical characterization is shown in Figure 1(d). The electrical characteristics of all devices were measured using an Agilent E5272A source/monitor unit in a N_2-filled glove box, in which both O_2 and H_2O values were below 0.1 ppm. A 635 nm laser source (fiber-coupled Fabry-Perot laser, S1FC635) was used as the light source when measuring the light current of the photodetector. The illumination area was confined to the active area of the OPD from the backside. The light intensity of the laser was calibrated by a Si photodiode (Hamamatsu S1133). To study the photodetector response time measurement, a DS345 function generator was used to generate square waveforms that controlled the light signal from a surface mounted LED (635 nm, LD1-R, LUXART® LED).

3. Photodetector architecture

As shown in Figure 1(a), the organic photodetector comprises a DG-OTFT and an OPD that are integrated and fabricated side by side on a common substrate. The DG-OTFT consists of an organic semiconductor layer, source and drain electrodes, a top-gate electrode with a top bilayer gate dielectric, and a bottom-gate electrode with a bottom-gate dielectric layer. The top bilayer gate dielectric comprises a first amorphous fluoropolymer layer and a second nanolaminate layer of two metal oxides (Al_2O_3 and HfO_2) deposited by atomic layer deposition (ALD). Since the DG-OTFT and the OPD are fabricated on the same ITO-coated substrate, the bottom-gate electrode of the transistor is electrically connected to the electron-collecting electrode (*i.e.*, bottom electrode) of the OPD. The hole-collecting electrode (*i.e.*, top electrode) of the OPD is grounded during operation. The photovoltage generated by the OPD under illumination is applied to the bottom-gate electrode of the DG-OTFT. The bottom-gate dielectric layer of the DG-OTFT has a high capacitance density of 151 nF cm^{-2} with a negligible loss tangent and thus a high resistance. Therefore, a very high load exists over the OPD causing it to operate close to open-circuit condition. Under illumination, the bottom-gate voltage (V_{BG}) of the OTFT can thus be considered as equal to

the open-circuit voltage (V_{OC}) of the OPD (*i.e.*, $V_{BG} = V_{OC}$). With fixed top-gate and drain-source voltages (V_{TG} and V_{DS}), the drain-source current (I_{DS}) changes with the V_{OC} produced by the incident optical power illuminating the OPD. Note that for this device to operate at low optical powers, the OPD must have a high shunt resistance (typically in the hundreds of GΩ range), otherwise parasitic currents flowing through the shunt resistance will prevent low-value photovoltages at low irradiance, limiting the sensitivity of the device.

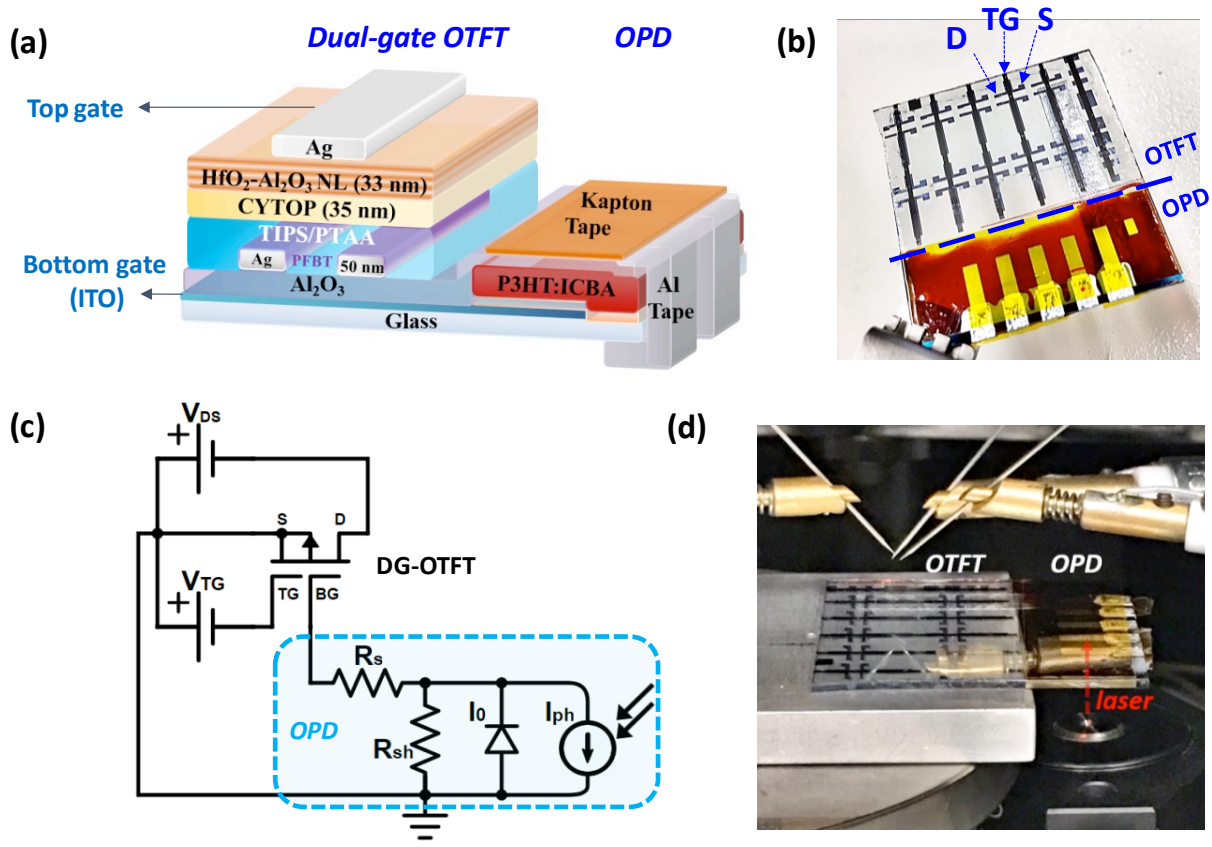

Figure 1. (a) The device structure of the novel organic photodetector that integrates a DG-OTFT and an OPD. (b) A photograph of the fabricated devices. (c) The circuit configuration of the photodetector. (d) A photograph of the device measurement setup.

To rationalize the merits of this structure, we first apply an analytical model by solving for the equivalent circuit shown in Figure 1(c). The model describes the conversion of the optical power absorbed by the OPD into a photovoltage and an expected source-drain current change that

is induced by this photovoltage onto the DG-OTFT. Following Prince's approach [26], the OPD is described through an equivalent circuit which comprises a diode with a reverse saturation current I_0, a photocurrent source I_{ph}, a series resistor R_s, and a shunt resistor R_p [27]. The I_{ph} corresponds to the photocurrent generated by the OPD under illumination.

Different from the conventional single-gate OTFT, the current-voltage characteristic of a DG-OTFT in a saturation regime (*i.e.*, $|V_{TG} - V_{th,eff} + V_{BG}(C_B/C_T)| \leq |(C_B + C_T)V_{DS}/C_T|$) is given by [28]:

$$I_{DS} = \frac{\mu}{2}\frac{W}{L}\frac{C_T^2}{C_T+C_B}\left(V_{TG} - V_{th,eff} + \frac{C_B}{C_T}V_{BG}\right)^2, \quad (1)$$

where μ is the field-effect carrier mobility, W is the channel width, L is the channel length, $V_{th,eff}$ is the effective threshold voltage, and C_T and C_B are the capacitance densities of the top- and bottom-gate dielectric, respectively. Since V_{OC}= V_{BG} = 0 V in the dark, I_{DS} reduces to:

$$I_{DS,dark} = \frac{\mu}{2}\frac{W}{L}\frac{C_T^2}{C_T+C_B}\left(V_{TG} - V_{th,eff}\right)^2. \quad (2)$$

Hence, under illumination, the light-induced change of channel current (ΔI_{DS}) equals: $I_{DS,light} - I_{DS,dark}$, which can be written as:

$$\Delta I_{DS} = I_{DS,light} - I_{DS,dark} = k_1[(k_2V_{OC})^2 + 2k_2V_{OC}\left(V_{TG} - V_{th,eff}\right)], \quad (3)$$

where $k_1 = \mu\,(W/L)\,[C_T^2/(2(C_T + C_B))]$ and $k_2 = C_B/C_T$. Note that under illumination, the photoresponse can be engineered to provide substantial amplification by selecting semiconducting materials (*i.e.,* larger μ values) and increasing the W/L ratio of the DG-OTFT.

Using a single-diode equivalent circuit model to describe the OPD, the relation of V_{OC} and photocurrent density J_{ph} of the OPD is given by [27]:

$$V_{OC} = n_{id}\frac{k_B T}{q}\ln[1 + \frac{J_{ph}}{J_0}(1 - \frac{V_{OC}}{J_{ph}R_p A})], \quad (4)$$

where q is the elementary charge, $k_B T$ is the thermal energy, J_0 is the reverse saturation current density of the diode, and n_{id} is the ideality factor of the diode. The value of J_{ph} is proportional to the incident optical power P_{opt}, *i.e.*, $J_{ph} = \eta(\lambda q/hc)(P_{opt}/A)$, where η is the external quantum efficiency, hc/λ is the incident photon energy, and A is the active area of the device. From equations (3) and (4), the effective responsivity $\Re$ can be written as:

$$\Re = \frac{\Delta I_{DS}}{P_{opt}} = \frac{|k_1[(k_2 V_{OC})^2 + 2k_2 V_{OC}(V_{TG} - V_{th,eff})]|}{P_{opt}}, \quad (5)$$

where $V_{OC} = \varphi_1 \ln(1 + \varphi_2 P_{opt} - \varphi_3 V_{OC})$. The parameters $\varphi_1 = n_{id}k_B T/q$, $\varphi_2 = \eta\lambda q/(hcAJ_0)$, and $\varphi_3 = 1/(J_0 R_p A)$. The values of φ_1, φ_2, and φ_3 can be obtained by fitting the experimental data.

From equation (5), we observe that the value of $\Re$ depends on the top-gate voltage V_{TG}, which provides the gain of a DG-OTFT. Equation (5) is valid in a saturation regime where V_{TG} is greater than $V_{th,eff}$. The photodetector shows the smallest values of $\Re_{min}$, when $V_{TG} = V_{th,eff}$. Thus, gain $Gain^{(V_{TG})}$, which is caused by V_{TG}, is given by:

$$Gain^{(V_{TG})} = \frac{\Re}{\Re_{min}} = 1 + \frac{2(V_{TG} - V_{th,eff})}{k_2 V_{OC}}. \quad (6)$$

When $V_{TG} = V_{th,eff}$, the value of $Gain^{(V_{TG})}$ equals to 1.

4. Results and discussions

The electrical characteristics of the photodetector were first measured in the dark. Figure 2(a) and (b) show the transfer and output characteristics, respectively, of the DG-OTFT in the dark. This data shows the channel's current modulation, which is only produced by the voltage applied to the top-gate electrode. The transfer characteristics were measured by sweeping V_{TG} from 2 V to -10 V and back, revealing negligible hysteresis in these DG-OTFTs. The output characteristics demonstrate that I_{DS} is independent with V_{DS} for values larger than 3 V and as expected, primarily controlled by the value of V_{TG} in the saturation region. Figure 2(c) shows the $|I_{ph}|$ dependence of the V_{OC} measured with a diode laser emitting at 653 nm for optical power values in the range between 20 pW and 4 mW. This data demonstrates that equation (4) properly describes the V_{OC} dependence on $|I_{ph}|$ over the entire range of optical power values studied and is consistent with the detailed characterization of P3HT:ICBA OPDs recently reported [25].

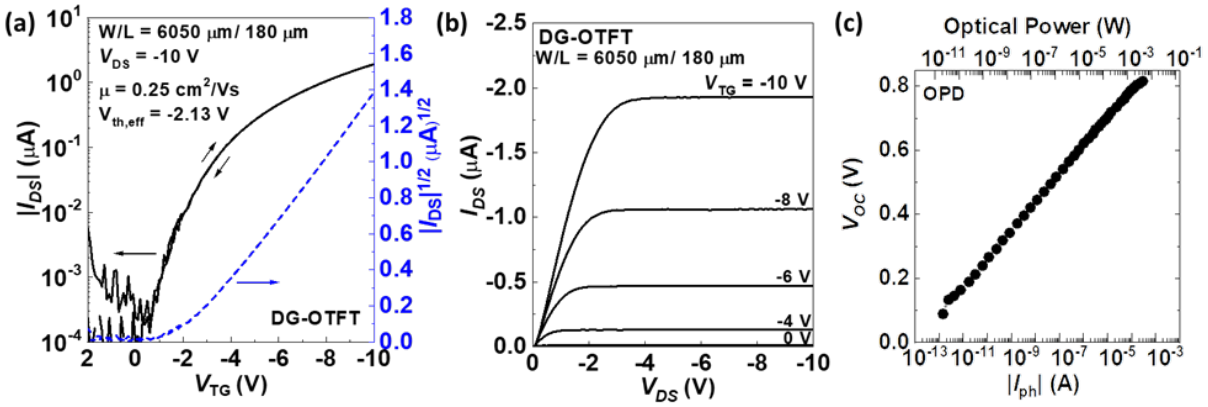

Figure 2. (a) The transfer characteristic and (b) output characteristic of a DG-OTFT in the dark. (c) Photovoltage produced by the OPD as a function of incident optical power and corresponding generated photocurrent.

Next, the characteristics under illumination were investigated using a 635 nm fiber-coupled laser source to illuminate the OPD from the ITO side, when the device was under a constant bias of V_{TG} = -10 V and V_{DS}= -6 V. Figure 3(a) compares the temporal characteristics of $|I_{DS}|$ in the dark and under varying illumination with increasing optical power in the range from 8 nW to 4 μW. In all conditions, the current was found to be stable. The inset of Figure 3(b) shows the measured and modeled dependence of $|\Delta I_{DS}|$ on the incident optical power from which the effective responsivity in Figure 3(b) is derived as $\Re = |\Delta I_{DS}|/P_{opt}$. Modeled values are calculated using equation (5). Effective responsivity values of 12 A W^{-1} at P_{opt}= 10^{-8} W are estimated following this approach. Modeled values are in good agreement with experimental data and show that the effective responsivity is nearly constant and reaches values as large as 30 A W^{-1} for weak optical powers < 1 nW. A constant responsivity means that the photocurrent will be linear with the optical power. Although limitations with the experimental setup did not allow the response of the photodetector to be studied for optical power values below 10 nA, it should be noted that data on Figure 2(c) supports the validity of the model down to optical power values ca. tens of picowatts. Furthermore, since the median noise equivalent power (*NEP*) of P3HT:ICBA OPDs can reach values of 230 fW at 525 nm [25], an extrapolation using responsivity values at the *NEP* suggests that the model should be accurate down to optical power values in the few picowatts range at 650 nm; and below these values at the peak of the OPD responsivity, in the range between ca. 500 and 600 nm. Values for the constants φ_1, φ_2, and φ_3 that are used to fit the data are presented in the table in Figure 3(c), together with other device parameters and bias voltages.

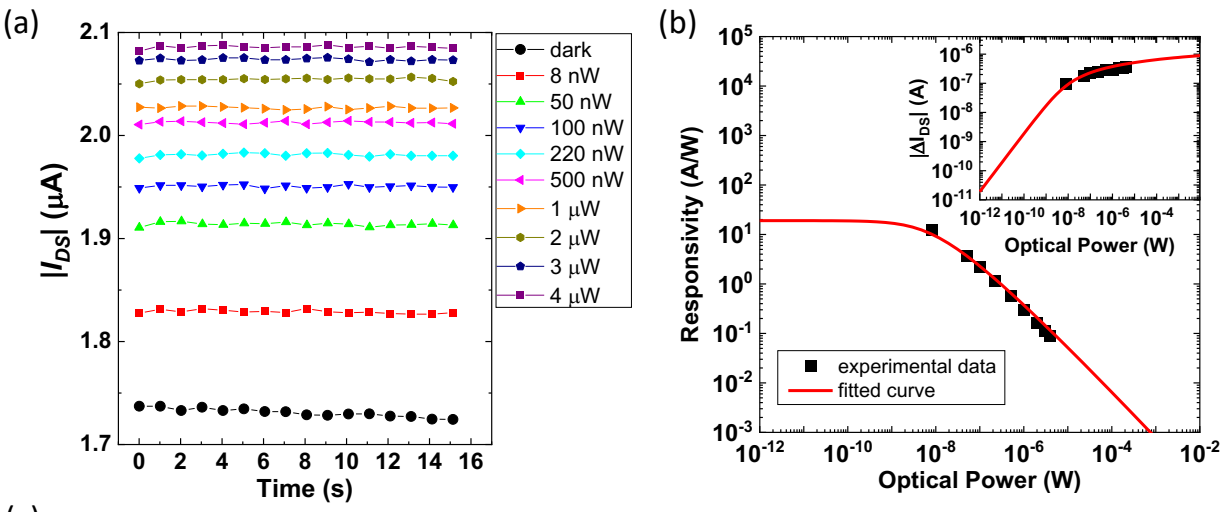

(c)

Device Parameters						Bias Voltages		Model Parameters		
W (μm)	L (μm)	μ ($cm^2V^{-1}s^{-1}$)	C_T ($nF\ cm^{-2}$)	C_B ($nF\ cm^{-2}$)	$V_{th,eff}$ (V)	V_{TG} (V)	V_{DS} (V)	ϕ_1 (V)	φ_2 (W^{-1})	φ_3 ($\Omega^{-1}A^{-1}$)
6050	180	0.25	37.2	150.6	-2.13	-10	-6	0.035	3.0×10^8	2.5

Figure 3. (a) $|I_{DS}|$ of the OTFT under constant bias voltages (V_{TG} = -10 V, V_{DS} = -6 V), when the top electrode of the OPD is grounded. The measurement was conducted in dark and irradiation with different incident optical power. (b) The responsivity of the photodetector versus incident optical power. The inset shows the changes of I_{DS} versus incident optical power. (c) A summary of device parameters.

The high values of the effective responsivity of this new photodetector are a result of the gain from the DG-OTFT under different gate biases. The values of gain versus optical power are shown in Figure 4(a), using equation (6) and the parameters in Figure 3(c). When the applied top-gate voltage V_{TG} equals to $V_{th,eff}$, the value of $Gain^{(V_{TG})}$ equals to 1 over the range of optical powers. When $|V_{TG}|$ is larger than $|V_{th,eff}|$, the value of $Gain^{(V_{TG})}$ increases by several orders, especially at low optical power range. Having validated our model, we conduct a numerical exercise to estimate how much the effective responsivity could be increased by optimizing the DG-OTFT. Using equation (5), we simulated the effective responsivity versus optical power by varying $\mu * W/L$ (*i.e.*, varying $k_1 \propto \mu * W/L$). All other parameters values corresponded to those in Figure 3(c). Figure 4(b) shows the result of simulating the effective responsivity versus optical

power with $\mu * W/L = K \times 8.5$ cm^2 V^{-1} s^{-1} with K in the range from 1 to 10^4. These simulations show that the responsivity could be further increased to values up 10^5 A W^{-1} by increasing $\mu\, W/L$ of the DG-OTFT by 10^4. For example, the channel's aspect ratio W/L can be increased to 2.5 × 10^5 for a 1 × 1 cm^2 DG-OTFT having interdigitated electrodes with a 10 µm channel length and a 30 µm linewidth [29, 30]. Also, using organic semiconductors with higher charge mobility could further boost the effective responsivity. As recently reviewed in reference [31], state-of-the-art solution-processed organic semiconductors can now reach charge mobility values of 20 cm^2 V^{-1} s^{-1}, around 80 times larger than that measured in our DG-OTFTs (μ = 0.25 cm^2 V^{-1} s^{-1}). Hence, based on current materials and printing methods, this approach could yield photodetectors with an effective responsivity of ca. 10^5 A W^{-1}.

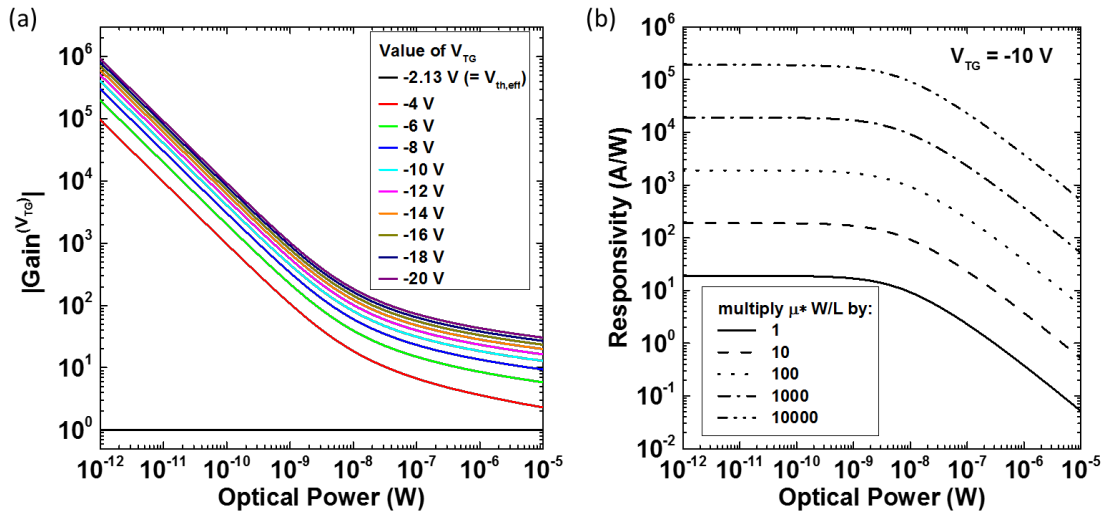

Figure 4. (a) The simulation of $Gain^{(V_{TG})}$ versus incident optical power with different V_{TG}. (b) The simulation of responsivity versus incident optical power with increased values of $\mu\, W/L$ (as presented in Figure 3(c)) by 1 to 10^4 times. In each simulation, the other parameters are fixed to the values in Figure 3(c).

Next, the photodetector's response time was evaluated. Figure 5 shows the normalized I_{DS} changes measured under the illumination of a red LED at 635 nm and modulated with a square waveform having a frequency of 0.2 Hz, 1 Hz, and 5 Hz with the OTFT biased at V_{TG} = -10 V and

V_{DS}= -6 V. The current measurement step size is 15 ms, which is the resolution of the source-meter equipment (Agilent E5272A). As it is clear from these data, the rise and fall time of the I_{DS} waveform is shorter than the measurement resolution, suggesting that the response frequency of the photodetector is higher than 67 Hz, which is compatible with video rate requirements.

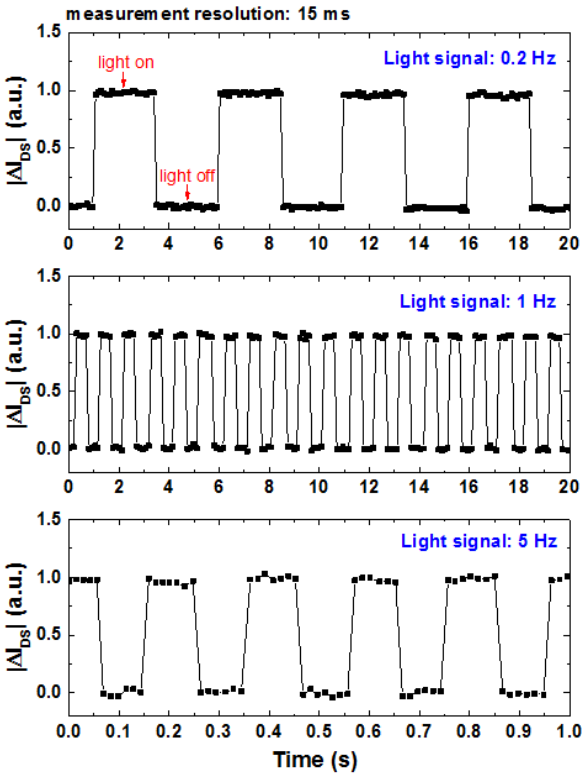

Figure 5. Response of I_{DS} changes under LED illumination at different on/off frequencies and with optical power values ca. 1 µW.

5. Conclusions

In summary, we demonstrated an organic photodetector with a configuration that integrates a DG-OTFT and an OPD. The DG-OTFT exhibits a small leakage current (around 0.1 nA) without hysteresis and good operational stability. A responsivity of 10 A W^{-1} at low optical power around 10^{-8} W is demonstrated, with short response time (< 15 ms). In order to study the device working principle, we used an analytic model, which shows great agreement with the measurement data obtained from the devices used in this work. As such, our results represent a proof-of-principle of the operation of a novel photodetector architecture. Based on these results, a simple approach to further improve the responsivity, especially at low optical power, was discussed. By further reducing the channel length *L*, increasing the channel width *W*, and using an organic semiconductor in the DG-OTFT that yields a larger field-effect mobility, the responsivity can be effectively scaled up by several hundreds to several thousand times. This result further confirms that the photodetector device with the new structure has great potential to ease the measurement of weak optical signals with optical power values in a range relevant for light detection and ranging (LIDAR), biomedical monitoring, fluorescence spectroscopy among many others. In addition, we believe that this photodetector geometry could be more easy integrated into flexible and large area photodetector arrays with high sensitivity to weak optical signals than a hybrid device consisting of an organic photodetector and an operational amplifier.

AUTHOR INFORMATION

Corresponding Author

*B. Kippelen. Email: kippelen@gatech.edu

Funding Sources

This research was supported in part by the Center for Organic Photonics and Electronics at Georgia Tech, by the Department of the Navy, Office of Naval Research Award No. N00014-14-1-0580 and N00014-16-1-2520, through the MURI Center for Advanced Photovoltaics (CAOP), by the Air Force Office of Scientific Research through Award No. FA9550-16-1-0168, by the Department of Energy/ National Nuclear Security Administration Awards No. DE-NA0002576 through the Consortium for Nonproliferation Enabling Technologies (CNEC) and No. DE-NA0003921 through the Consortium Enabling Technologies and Innovation (ETI).

Declaration of Interests

The authors declare that they have no known competing financial interests or personal relationships that could have appeared to influence the work reported in this paper.

References:

1. Chow, P. C. Y.; Someya, T., Organic Photodetectors for Next-Generation Wearable Electronics. Adv. Mater. 32, (2019)**,** 1902045. https://doi.org/10.1002/adma.201902045

2. Ballard, Z. S.; Ozcan, A., Wearable Optical Sensors. In *Mobile Health: Sensors, Analytic Methods, and Applications*, Rehg, J. M.; Murphy, S. A.; Kumar, S., Eds. Springer International Publishing: Cham, 2017; pp 313-342.

3. Zheng, Y. L.; Ding, X. R.; Poon, C. C. Y.; Lo, B. P. L.; Zhang, H.; Zhou, X. L.; Yang, G. Z.; Zhao, N.; Zhang, Y. T., Unobtrusive Sensing and Wearable Devices for Health Informatics. IEEE. Trans. Biomed. Eng. 61, (2014)**,** 1538-1554. https://doi.org/10.1109/TBME.2014.2309951

4. Perera, C.; Zaslavsky, A.; Christen, P.; Georgakopoulos, D., Context Aware Computing for The Internet of Things: A Survey. IEEE Commun. Surv. Tut. 16, (2014)**,** 414-454. https://doi.org/10.1109/SURV.2013.042313.00197

5. Ghanbarzadeh, S.; Abbaszadeh, S.; Karim, K. S., Low Dark Current Amorphous Silicon Metal-Semiconductor-Metal Photodetector for Digital Imaging Applications. IEEE Electron Device Lett. 35, (2014)**,** 235-237. https://doi.org/10.1109/LED.2013.2295976

6. Eppeldauer, G.; Hardis, J. E., Fourteen-decade photocurrent measurements with large-area siliconphotodiodes at room temperature. Appl. Opt. 30, (1991)**,** 3091-3099. https://doi.org/10.1364/AO.30.003091

7. Fuentes-Hernandez, C.; Chou, W.-F.; Khan, T. M.; Diniz, L.; Lukens, J.; Larrain, F. A.; Rodriguez-Toro, V. A.; Kippelen, B., Large-area low-noise flexible organic photodiodes for detecting faint visible light. accepted for publication in Science, (2020).

8. de Arquer, F. P. G.; Armin, A.; Meredith, P.; Sargent, E. H., Solution-processed semiconductors for next-generation photodetectors. Nat. Rev. Mat. 2, (2017), 16100. https://doi.org/10.1038/natrevmats.2016.100

9. Saracco, E.; Bouthinon, B.; Verilhac, J.-M.; Celle, C.; Chevalier, N.; Mariolle, D.; Dhez, O.; Simonato, J.-P., Work Function Tuning for High-Performance Solution-Processed Organic Photodetectors with Inverted Structure. Adv. Mater. 25, (2013), 6534-6538. http://dx.doi.org/10.1002/adma.201302338

10. Congreve, D. N.; Lee, J.; Thompson, N. J.; Hontz, E.; Yost, S. R.; Reusswig, P. D.; Bahlke, M. E.; Reineke, S.; Van Voorhis, T.; Baldo, M. A., External Quantum Efficiency Above 100% in a Singlet-Exciton-Fission–Based Organic Photovoltaic Cell. Science 340, (2013), 334-337. https://doi.org/10.1126/science.1232994

11. Dou, L.; Yang, Y.; You, J.; Hong, Z.; Chang, W.-H.; Li, G.; Yang, Y., Solution-processed hybrid perovskite photodetectors with high detectivity. Nat. Commun. 5, (2014), 5404. http://dx.doi.org/10.1038/ncomms6404

12. Jansen-van Vuuren, R. D.; Armin, A.; Pandey, A. K.; Burn, P. L.; Meredith, P., Organic Photodiodes: The Future of Full Color Detection and Image Sensing. Adv. Mater. 28, (2016), 4766-4802. http://dx.doi.org/10.1002/adma.201505405

13. Miao, J.; Zhang, F., Recent Progress on Photomultiplication Type Organic Photodetectors. Laser Photon. Rev. 13, (2019), 1800204. https://doi.org/10.1002/lpor.201800204

14. Xu, H.; Li, J.; Leung, B. H. K.; Poon, C. C. Y.; Ong, B. S.; Zhang, Y.; Zhao, N., A high-sensitivity near-infrared phototransistor based on an organic bulk heterojunction. Nanoscale 5, (2013), 11850-11855. http://dx.doi.org/10.1039/C3NR03989G

15. Pierre, A.; Gaikwad, A.; Arias, A. C., Charge-integrating organic heterojunction phototransistors for wide-dynamic-range image sensors. Nat Photon 11, (2017), 193-199. http://dx.doi.org/10.1038/nphoton.2017.15

16. Loffredo, F.; Bruno, A.; Del Mauro, A. D. G.; Grimaldi, I. A.; Miscioscia, R.; Nenna, G.; Pandolfi, G.; Petrosino, M.; Villani, F.; Minarini, C.; Facchetti, A., Photoresponse of pentacene-based transistors. Phys. Status Solidi (a) 211, (2014), 460-466. https://doi.org/10.1002/pssa.201300395

17. Singh, S.; Mohapatra, Y. N., Persistent photocurrent (PPC) in solution-processed organic thin film transistors: Mechanisms of gate voltage control. J. Appl. Phys. 120, (2016), 045501. http://aip.scitation.org/doi/abs/10.1063/1.4959823

18. Liu, X.; Lee, E. K.; Kim, D. Y.; Yu, H.; Oh, J. H., Flexible Organic Phototransistor Array with Enhanced Responsivity via Metal–Ligand Charge Transfer. ACS Appl. Mater. Inter. 8, (2016), 7291-7299. http://dx.doi.org/10.1021/acsami.5b11523

19. Nam, H. J.; Cha, J.; Lee, S. H.; Yoo, W. J.; Jung, D.-Y., A new mussel-inspired polydopamine phototransistor with high photosensitivity: signal amplification and light-controlled switching properties. Chem. Comm. 50, (2014), 1458-1461. http://dx.doi.org/10.1039/C3CC48309F

20. Baeg, K.-J.; Binda, M.; Natali, D.; Caironi, M.; Noh, Y.-Y., Organic Light Detectors: Photodiodes and Phototransistors. Adv. Mater. 25, (2013), 4267-4295. http://dx.doi.org/10.1002/adma.201204979

21. Someya, T.; Kato, Y.; Shingo, I.; Noguchi, Y.; Sekitani, T.; Kawaguchi, H.; Sakurai, T., Integration of organic FETs with organic photodiodes for a large area, flexible, and lightweight sheet image scanners. IEEE Trans. Electron Devices 52, (2005), 2502-2511. https://doi.org/10.1109/TED.2005.857935

22. Jia, X.; Fuentes-Hernandez, C.; Wang, C.-Y.; Park, Y.; Kippelen, B., Stable organic thin-film transistors. Sci. Adv. 4, (2018), eaao1705. https://doi.org/10.1126/sciadv.aao1705

23. Wang, C.-Y.; Fuentes-Hernandez, C.; Chou, W.-F.; Kippelen, B., Top-gate organic field-effect transistors fabricated on paper with high operational stability. Org. Elec. 41, (2017), 340-344. https://doi.org/10.1016/j.orgel.2016.11.026

24. Wang, C.-Y.; Fuentes-Hernandez, C.; Yun, M.; Singh, A.; Dindar, A.; Choi, S.; Graham, S.; Kippelen, B., Organic Field-Effect Transistors with a Bilayer Gate Dielectric Comprising an Oxide Nanolaminate Grown by Atomic Layer Deposition. ACS Appl. Mater. Inter. 8, (2016), 29872-29876. http://dx.doi.org/10.1021/acsami.6b10603

25. Fuentes-Hernandez, C.; Chou, W.-F.; Khan, T. M.; Diniz, L.; Lukens, J.; Larrain, F. A.; Rodriguez-Toro, V. A.; Kippelen, B., Large-area low-noise flexible organic photodiodes for detecting faint visible light. Science 370, (2020), 698. https://doi.org/10.1126/science.aba2624

26. Prince, M. B., Silicon Solar Energy Converters. J. Appl. Phys. 26, (1955), 534-540. https://doi.org/10.1063/1.1722034

27. Kippelen, B.; Bredas, J. L., Organic photovoltaics. Energy Environ. Sci. 2, (2009), 251. http://dx.doi.org/10.1039/b812502n

28. Abe, K.; Takahashi, K.; Sato, A.; Kumomi, H.; Nomura, K.; Kamiya, T.; Kanicki, J.; Hosono, H., Amorphous In–Ga–Zn–O Dual-Gate TFTs: Current–Voltage Characteristics and Electrical Stress Instabilities. IEEE Trans. Electron Devices 59, (2012), 1928-1935. https://doi.org/10.1109/TED.2012.2195008

29. Fukuda, K.; Someya, T., Recent Progress in the Development of Printed Thin-Film Transistors and Circuits with High-Resolution Printing Technology. Adv. Mater. 29, (2017), 1602736. https://doi.org/10.1002/adma.201602736

30. Chung, S.; Ha, J.; Hong, Y., Fully inkjet-printed short-channel organic thin-film transistors and inverter arrays on flexible substrates. Flex. Print. Electron. 1, (2016), 045003. http://dx.doi.org/10.1088/2058-8585/1/4/045003

31. Paterson, A. F.; Singh, S.; Fallon, K. J.; Hodsden, T.; Han, Y.; Schroeder, B. C.; Bronstein, H.; Heeney, M.; McCulloch, I.; Anthopoulos, T. D., Recent Progress in High-Mobility Organic Transistors: A Reality Check. Adv. Mater. 30, (2018), 1801079. https://doi.org/10.1002/adma.201801079